Am J Physiol Renal Physiol 308: F661–F670, 2015.
First published January 13, 2015; doi:10.1152/ajprenal.00022.2014.

CALL FOR PAPERS | *Renal Hemodynamics: Integrating with the Nephron and Beyond*

Laser speckle contrast imaging reveals large-scale synchronization of cortical autoregulation dynamics influenced by nitric oxide

Nicholas Mitrou,[1] Christopher G. Scully,[2] Branko Braam,[3] Ki H. Chon,[2] and William A. Cupples[1]

[1]*Department of Biomedical Physiology and Kinesiology, Simon Fraser University, Burnaby, British Columbia, Canada;* [2]*Department of Biomedical Engineering, Worcester Polytechnic Institute, Worcester, Massachusetts; and* [3]*Department of Medicine and Department of Physiology, University of Alberta, Edmonton, Alberta, Canada*

Submitted 10 January 2014; accepted in final form 8 January 2015

Mitrou N, Scully CG, Braam B, Chon KH, Cupples WA. Laser speckle contrast imaging reveals large-scale synchronization of cortical autoregulation dynamics influenced by nitric oxide. *Am J Physiol Renal Physiol* 308: F661–F670, 2015. First published January 13, 2015; doi:10.1152/ajprenal.00022.2014.—Synchronization of tubuloglomerular feedback (TGF) dynamics in nephrons that share a cortical radial artery is well known. It is less clear whether synchronization extends beyond a single cortical radial artery or whether it extends to the myogenic response (MR). We used LSCI to examine cortical perfusion dynamics in isoflurane-anesthetized, male Long-Evans rats. Inhibition of nitric oxide synthases by N^{ω}-nitro-L-arginine methyl ester (L-NAME) was used to alter perfusion dynamics. Phase coherence (PC) was determined between all possible pixel pairs in either the MR or TGF band (0.09–0.3 and 0.015–0.06 Hz, respectively). The field of view (≈4 × 5 mm) was segmented into synchronized clusters based on mutual PC. During the control period, the field of view was often contained within one cluster for both MR and TGF. PC was moderate for TGF and modest for MR, although significant in both. In both MR and TGF, PC exhibited little spatial variation. After L-NAME, the number of clusters increased in both MR and TGF. MR clusters became more strongly synchronized while TGF clusters showed small highly coupled, high-PC regions that were coupled with low PC to the remainder of the cluster. Graph theory analysis probed modularity of synchronization. It confirmed weak synchronization of MR during control that probably was not physiologically relevant. It confirmed extensive and long-distance synchronization of TGF during control and showed increased modularity, albeit with larger modules seen in MR than in TGF after L-NAME. The results show widespread synchronization of MR and TGF that is differentially affected by nitric oxide.

kidney; cortex; blood flow; dynamics; synchronization; laser speckle contrast imaging; rats; myogenic response; tubuloglomerular feedback

TUBULOGLOMERULAR FEEDBACK (TGF) and the myogenic response (MR) are the canonical mechanisms that mediate autoregulation of renal blood flow (RBF). Both mechanisms control the diameter of the afferent arteriole to change preglomerular vascular resistance, and both contribute to gain of autoregulation (18, 24, 51). Although autoregulation is mostly considered in the context of each individual nephron and its afferent arteriole responding to changes in blood pressure (BP) (16), this view is being superseded by the increasing recognition that the microcirculation in many beds operates as a set of distributed networks (4, 26, 32, 33). In such a network, all vessel segments contribute to determining flow in any one vessel; restated, this says that regulation of flow requires coordination of resistance changes along multiple segments in any given pathway (33).

In the kidney, it is clear that TGF is synchronized in nephron pairs and triplets supplied by the same cortical radial artery (19), that this synchronization could contribute to the efficacy of autoregulation (25), and that some hypertensive models display altered synchronization of TGF (11, 52). The MR also shows synchronized dynamics in nephron pairs and triplets (41). Both TGF (47) and the MR (34) are vascular conducted responses whereby constriction or dilatation is conducted along the endothelium of a blood vessel with length constants ~300 μm (47), or roughly twice the length of an afferent arteriole (10). These findings suggest that synchronization of TGF involves, at a minimum, all 15–20 nephrons in a lobule. However, there is little evidence in the literature of synchronization of either TGF or MR at the scale of the lobule or larger, due at least in part to the inability to study more than two or three nephrons simultaneously. While there are data in the literature that are consistent with wide-scale synchronization of MR, they do not demonstrate the phenomenon (13). Recently, laser speckle contrast imaging (LSCI) has been shown to capture the dynamics of renal autoregulation at the cortical surface (21, 36, 37). Holstein-Rathlou et al. (21) identified strong synchronization of TGF dynamics in small groups of efferent arterioles (up to $n = 7$) and interpreted the data in terms of local synchronization.

Scully et al. (36) showed that renal surface perfusion can be segmented into clusters based upon synchronized MR dynamics and that these clusters are surprisingly large. The importance of addressing MR dynamics is that failure of myogenic autoregulation and development of renal failure have been closely linked both functionally and genetically (8, 28), thus providing strong evidence that the MR is both necessary and sufficient for effective autoregulation.

Here, we report studies designed to assess synchronization of both mechanisms over larger scales than previously, from the lobule (≈0.6-mm diameter) to the field of view (≈4 × 5

Address for reprint requests and other correspondence: W. A. Cupples, Dept. of Biomedical Physiology and Kinesiology, Simon Fraser Univ., 8888 University Dr., Burnaby, BC, Canada V5A 1S6E-M (e-mail: wcupples@sfu.ca).

 1931-857X/15 Copyright © 2015 the American Physiological Society

Downloaded from www.physiology.org/journal/ajprenal by ${individualUser.givenNames} ${individualUser.surname} (137.099.170.116) on September 1, 2018.
Copyright © 2015 American Physiological Society. All rights reserved.

mm) or 50–60 lobules. The accessible kidney surface was segmented into synchronized regions (clusters) by phase coherence between all possible pairs of pixels from the imaged surface (27 × 37 pixels). A subsequent analysis using graph theory probed modularity of MR and TGF synchronization (30). N^{ω}-nitro-L-arginine methyl ester (L-NAME) was used to increase renal vascular tone and change autoregulation dynamics, actions that are largely independent of BP (39, 48–50). The results show widespread moderate (TGF) or weak (MR) synchronization that is substantially and differentially altered by inhibition of nitric oxide synthases.

Table 1. *Hemodynamic variables*

Variable	Control	L-NAME	*P*
BP, mmHg	100 ± 5	130 ± 3	0.0015
RBF, ml/min	7.0 ± 0.7	4.4 ± 0.5	0.0005
G, ml·min^{-1}·mmHg^{-1}	0.071 ± 0.009	0.033 ± 0.004	0.0003
LS flux, AU	1,600 ± 30	990 ± 80	0.0011
LS *G*, AU/mmHg	16 ± 1	7.5 ± 0.6	<0.0001

Values are means ± SE. Shown are hemodynamic data during control period and after N^{ω}-nitro-L-arginine methyl ester (L-NAME). BP, mean blood pressure; RBF, renal blood flow; *G*, renal vascular conductance; LS flux, laser speckle perfusion; LS *G*, laser speckle perfusion conductance.

METHODS

All experiments were approved by the Animal Care Committee of Simon Fraser University and performed according to the guidelines of the Canadian Council on Animal Care. Male Long-Evans rats (age 12–14 wk, $n = 7$) were purchased from Charles River, Canada (St. Hyacinthe, QC) or Harlan Laboratories (Livermore, CA) and housed in groups of three to five with ad libitum access to standard rat chow and distilled water.

Each rat received the analgesic buprenorphine (0.02 mg/kg sc, Summit Veterinary Pharmacy, Aurora, ON) 20 min before anesthesia. Anesthesia was induced with 4% isoflurane (Aerrane; Baxter, Mississauga, ON) in inspired air (45% O_2). After induction, the rat was transferred to a heated surgical table (35°). The trachea was cannulated (PE-210), and the rat was ventilated with a pressure-controlled small animal ventilator (TOPO, Kent Scientific, Torrington, CT) operating in timed ventilation mode and adjusted to match the rat's natural breathing rate (50–60/min). During surgery, inspired isoflurane was set to 2%.

The left femoral vein was cannulated (PE-50) for infusion of 2% charcoal-washed bovine serum albumin (Sigma-Aldrich, Oakville, ON) in normal saline at 1% body wt/h. The left femoral artery was cannulated (PE-90 with a narrowed tip) and connected to a pressure transducer (TRN050, Kent) driven by a TRN005 amplifier for measurement of BP. The left kidney was exposed by a subcostal flank incision, freed from surrounding fat, and placed in a plastic cup mounted to the surgical table. The kidney was embedded in silicone stopcock grease (Dow Corning, Midland, MI) to minimize motion. After the renal artery was stripped, a transit time ultrasound flow probe (PRB-001, Transonic Systems, Ithaca, NY) was attached. The flow probe was secured in place with acoustic coupling gel (NALCO 1181 and surgical lubricant) and driven by a TS420 flowmeter (Transonic). Except during data acquisition, the surface of the kidney was covered with Parafilm to prevent drying. Anesthesia was reduced to the lowest dose (~1.5%) that prevented BP responses to toe pinching, and the animal was allowed to stabilize for 1 h.

The kidney surface was cleaned with normal saline and periodically moistened thereafter. LSCI was performed with a Moor FLPI laser speckle contrast imager (Moor Instruments, Axminster, UK) positioned ≈18 cm above the kidney surface. The instrument was modified by the manufacturer to have twice the optical zoom of the standard model, permitting a small field of view (≈4 × 5 mm) (Table 1). Approximately one-third of the dorsal surface was imaged.

To avoid aliasing heart rate-dependent flow pulses into perfusion (35), the imager was used in spatial averaging mode which acquires 113 × 152-pixel images of perfusion at 25 Hz. Before each record was taken, a 4-mm hair was placed on the surface to determine pixel size and to assist in focusing the LSCI camera.

Experiments. Previous studies showed that record lengths of 30–50 cycles (300 s) are required to probe MR synchronization (36), and pilot studies showed the same 30- to 50-cycle (1,500 s) requirement for probing TGF synchronization. BP, RBF, and LSCI signals were acquired during spontaneous BP fluctuation before and after injection of L-NAME (Sigma, 10 mg/kg iv) in 10 rats. Three animals were removed from analysis due to lack of L-NAME-dependent vasoconstriction ($n = 1$) or lack of a detectable myogenic dynamic in RBF ($n = 2$), leaving seven animals for full analysis.

Synchronization and cluster analysis. Synchronization of oscillators can be addressed by assessment of phase locking or of frequency entrainment (31); however, phase locking is the standard definition of synchronization (1, 31). Thus determination of synchronization on the surface of the kidney used methods described in detail elsewhere (36) that are based on assessment of the stability in time of phase relationships among pixels. Briefly, each image was filtered with a Gaussian spatial filter (8-pixel width) and then down-sampled by a factor of 4, yielding a 27 × 37-pixel image for each frame with average pixel size of 135 × 135 μm (36, 37). The TGF (0.015–0.06 Hz) and MR (0.09–0.3 Hz) frequency ranges were isolated by a bandpass forward-backward Butterworth filter so that phase information was preserved. Then, the Hilbert transform of the data was used to extract the instantaneous phase. The Hilbert transform of a real number produces a complex number, the arc tangent of which is the instantaneous phase of the oscillation. Synchronization was assessed by calculating the phase coherence (PC; *Eq.1*) between all possible pairs of imaged pixels.

$$\mathrm{PC}_{jk} = \left| \frac{1}{N} \sum_{m=1}^{N} e^{i(\phi_j - \phi_k)} \right| \qquad (1)$$

where PC_{jk} is the phase coherence between two pixels j and k, where N is the number of points in the original data, and ϕ_j and ϕ_k are the instantaneous phases of pixels j and k, respectively. It is the mean of the exponential difference between the instantaneous phases of two pixels over time. PC is bounded by 0 and 1, where PC = 0 means there is no relationship between the two pixels and PC = 1 indicates complete 1:1 phase locking.

A surrogate data approach was used to estimate PC that could be considered significant. For each pixel pair, PC was determined after a random circular phase shift was applied to one pixel. The significance threshold was set at two SD greater than the mean PC from 50 iterations of this procedure. Pixel pairs that had PC less than the threshold were considered to be nonsignificant. They were set to "not-a-number" and thereby excluded from further analyses. PC for TGF was computed over the entire 1,500-s record, while PC for MR was computed over 300-s segments with 50% overlap. We did this because the threshold for significance decreases as the number of cycles increases in a data set, so a similar number of cycles was used to analyze MR and TGF (36).

Calculating pairwise PC allows comparison of any particular, or reference, pixel to all other pixels in the field of view. Simply moving the reference pixel can give some indication of the presence and location of synchronized regions, but would be cumbersome and insensitive. Instead, we used cluster analysis of the PC values to determine the number of synchronized clusters and their location on the renal surface. From the available methods of clustering, we tested three and chose to use nonnegative matrix factorization (NMF) because it was the most accurate in the presence of high PC between clusters (35). We have described this procedure in detail (36). Briefly,

Downloaded from www.physiology.org/journal/ajprenal by ${individualUser.givenNames} ${individualUser.surname} (137.099.170.116) on September 1, 2018.
Copyright © 2015 American Physiological Society. All rights reserved.

the pairwise PC results were first transformed from a four-dimensional 27 × 37 × 27 × 37 matrix to a 999 × 999 synchronization matrix that held the PC values between all pairs of pixels. Then, we used NMF to estimate the number and location of synchronized clusters. NMF is an algorithm designed to approximate the $n \times n$ matrix V into two vectors, W ($n \times r$) and H ($r \times n$), where r is the number of clusters, so that *Eq. 2* is satisfied.

$$WH \approx V \tag{2}$$

The NMF calculation was iterated with increasing values of r, from 1 to 10, and the resulting error was computed after each iteration according to *Eq. 3*.

$$D = \|WH - V\|^2 \tag{3}$$

At the first error reduction <0.01 after increasing of r by 1, i.e., $D_{r+1} - D_r, < 0.01$, the number of clusters was set to r. For the chosen number of clusters r, the matrices W and H are used to determine the cluster that each pixel belongs to by finding the cluster m that produces the largest contribution to the estimate of V according to *Eq. 4*.

$$\text{Cluster}(m) = \arg\max_m (W_{nm} H_{mn}) \tag{4}$$

Cluster dimensions were estimated from the pixel dimensions in individual experiments and the number of pixels contained within each cluster. For this purpose, edges of the field of view were treated as cluster boundaries. Thus the estimates of cluster area must be considered as estimates at best and as lower limits, particularly when the number of clusters in the field of view was small.

PC between the geometric centroid of each cluster and all other significant pixels in the same cluster was used to provide an index of the overall strength of synchronization in each cluster. The absolute value of phase difference (PD) between two pixels provides an indication of the coupling mechanism. Low PD, near 0 radians (rad), suggests electrotonic coupling, whereas high PD, near π rad, suggests hemodynamic coupling. With spontaneous BP fluctuation, as in this study, the signal-to-noise ratio (SNR) can be low (35), so we tested the sensitivity of the Hilbert analysis described above and the wavelet-based approach that is described in detail (21) using the Morlet wavelet with an initial order of 6. We determined PC and PD between two identical sine waves ($f = 0.05$) to which Gaussian white noise was added to reduce SNR from +40 to −20 decibels (dB) in 1-dB decrements. To provide an estimate of variance, 100 iterations were performed at each SNR.

TGF clusters after L-NAME showed pronounced heterogeneity of PC and PD within clusters, suggesting that synchronization, at least in this condition, is modular in nature. Consequently, a secondary analysis based on graph theory was used to determine the extent of modularity within synchronized clusters. Modularity is an index of the group characteristics of a graph. Higher values of modularity indicate that groups of nodes within a graph have more intragroup edges than intergroup edges, which, in this case, would be consistent with stronger synchronization within cortical lobules rather than between them. To visualize the spatial organization of TGF and MR synchronization, we reconstructed the renal surface using graph theory (9, 14, 30). In this construct a graph $G(V,E)$ contains a set of nodes, V, and a set of edges, E. Each downsampled pixel was treated as a node and was connected to other nodes when significant PC (edges) existed between those pixels. Because the total number of edges with significant PC sometimes approached the limiting value (498, 501), we used one rat with no detectable myogenic signature in the BP-RBF transfer function to estimate an operational threshold for data presentation. It displayed a small number of edges, but none with PC >0.5. We therefore limited our analysis to edges having PC ≥0.6. For each graph, we also measured its modularity as described in detail by Newman (30).

Statistical analysis. Differences between experimental periods and between MR and TGF were assessed with paired *t*-tests. PC is bounded from 0 to 1 and thus not normally distributed and nor is modularity; thus differences in these variables were tested with the Wilcoxon signed-ranks test. Data analysis was performed in Matlab (r2013a, The Mathworks, Natick, MA), and statistical tests were performed in SPSS (v22, IBM, Armonk, NY). Data are shown as means ± SE, and $P < 0.05$ was considered statistically significant.

RESULTS

Table 1 reports BP, RBF, and LSCI for all seven rats, both before and after L-NAME. As expected L-NAME increased BP and reduced both RBF and LSCI ($P < 0.01$ in all cases). In this study, LSCI flux varied with RBF at 240 ± 45 AU·(ml/min)$^{-1}$.

Figure 1 shows a basic representation of the signals that were extracted from each LSCI image series. Figure 1*A* shows the flux across the renal surface averaged over 25 min. The

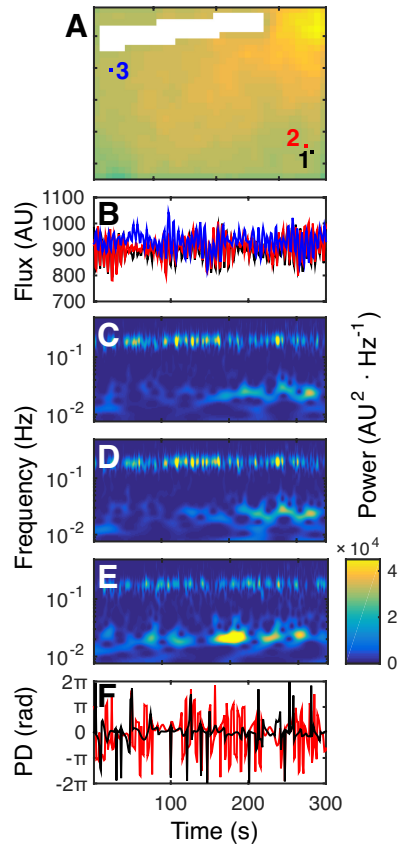

Fig. 1. *A*: laser speckle flux on a 5 × 7-mm area of the renal surface averaged over 1,500 s. Three regions of interest (ROI) are labeled *1–3*. The color of each label corresponds to the color of subsequent time series. *B*: time series of flux extracted from each ROI. Three hundred seconds are shown. Fluctuations in flux are similar between ROI 1 (black) and ROI 2 (red) but not between ROI 1 or ROI 2 and ROI 3 (blue). *C*: time-varying power spectrum from ROI 1. There are intermittent contributions of power from tubuloglomerular feedback (TGF) and myogenic response (MR). *D*: time-varying power in TGF and MR from ROI 2 are similar to and temporally aligned with equivalent events in the power spectrum from ROI 1 shown in *C*. *E*: power spectrum from ROI 3 shows fluctuations in power and contains information from both MR and TGF. However, the events that occur in ROI 3 are not similar in power or time to ROI 1 or ROI 2. *F*: difference in instantaneous phase in the myogenic range (0.09−0.3 Hz) between ROI 1 and 2 (black) and between ROI 1 and 3 (red). Phases were constrained to $[-\pi,\pi]$, so phase differences fell within $[-2\pi,2\pi]$. The small variation in phase difference between ROI 1 and ROI 2 is consistent with their synchronization whereas the much greater variation in phase difference between distant ROI 1 and ROI 3 suggests those ROIs are at most weakly synchronized.

Downloaded from www.physiology.org/journal/ajprenal by ${individualUser.givenNames} ${individualUser.surname} (137.099.170.116) on September 1, 2018.
Copyright © 2015 American Physiological Society. All rights reserved.

mean flux is not homogeneous across the surface and instead has a region of high flux at the *top right* that transitions to low flux in the *bottom left*. Figure 1*B* shows 300-s segments of filtered flux time series extracted from three single-pixel regions of interest (ROI; 0.037 mm^2), chosen so that two are neighbors (separated by 0.27 mm) and the third is remote from that pair. The waveforms of the two neighboring ROI appear similar whereas that of the remote ROI is visibly dissimilar. Time-varying spectral power was estimated by the wavelet transform of each ROI (37). Time-varying spectra for neighboring ROI (Fig. 1, *C* and *D*) show largely synchronous power fluctuation in both MR and TGF bands. In contrast, the time-varying spectrum of the remote ROI (Fig. 1*E*) shows clear temporal dissociation of power in MR and TGF. Figure 1*F* shows that PD between the neighboring ROI is stable near zero, suggesting a high degree of phase coherence, whereas distant ROI have rapidly fluctuating PD, suggesting no synchronization. PC between the two nearby ROI ($PC_{1,2}$) was 0.81, while $PC_{1,3}$ was 0.33 and $PC_{2,3}$ was 0.28. Although inspection of $PD_{1,2}$ shows it is close to zero, phase slips ($\pm 2\pi$) introduce noise so $PD_{1,2} > 0$ and $PC_{1,2} < 1$.

Figure 2 shows PC and PD determined for coherent sine waves with systematically varied SNR. As expected, in-phase sine waves uniformly had PC = 1 and PD = 0 rad whether determined by the Hilbert transform or by wavelets. At lower SNR, between ≈15 and 5 dB, the Hilbert analysis correctly identifies the existing synchronization, although with progressively degraded PC and PD. In contrast, the wavelet-based analysis correctly assigns PC and PD down to SNR ≈20 dB but fails to detect existing synchronization at lower SNR.

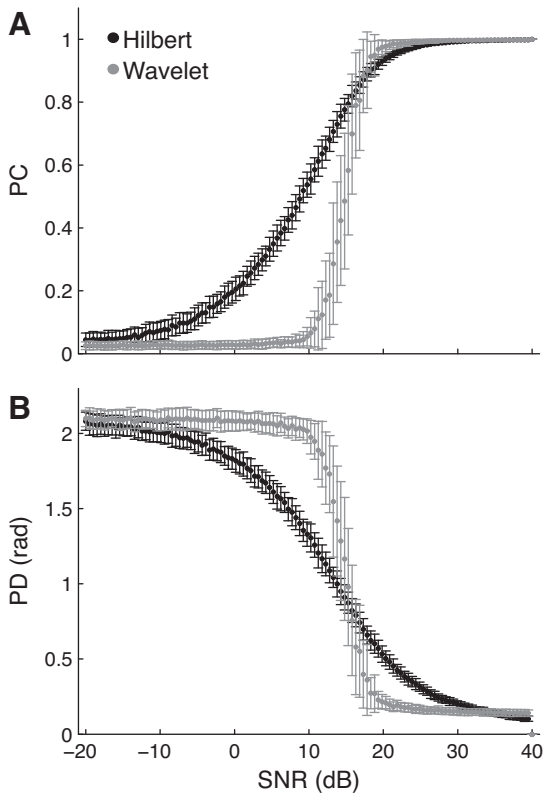

Fig. 2. Effect of white noise on phase coherence (PC; *A*) and phase difference (PD; *B*). Identical, in-phase sine waves have PC = 1 and PD = 0 rad when phase was detected using the Hilbert transform (black) or wavelet transform (grey). As signal-to-noise ratio (SNR; dB) is reduced from 40 to −20 dB, there is a sigmoid reduction in PC for Hilbert and wavelet. However, PC is reduced gradually as SNR decreases when Hilbert is used, whereas PC decreases rapidly to zero when SNR is <20 dB. Because the test sine waves are identical, the failure of the wavelet transform to detect PC is a false-negative result. Similarly, PD shows a sigmoid increase to the limiting value of 2.09 ± 0.03 rad for Hilbert and wavelet techniques, with a pattern similar to PC.

Figure 3 shows synchronization of MR in one rat before and after L-NAME. During the control period, portions of two clusters are visible in the field of view. PC in each cluster was modest, with mean PC = 0.50, and PD = 0.4π rad; both PC and PD were homogeneously distributed. The coefficient of variation of PC (CV_{PC}) was 10%, consistent with the even distribution of PC across the field of view. After L-NAME, the number of clusters increased from two to five and they had greater PC and lower PD than during the control period. Mean within-cluster PC after L-NAME was 0.67 in this animal while within-cluster PD was 0.3π rad. The edges of each cluster retained lower PC and higher PD, making the cluster boundaries clearly demarcated. The distribution of PC within clusters was altered so that the CV_{PC} increased to 19%.

MR synchronization in all seven rats showed similar patterns to results from the rat shown in Fig. 3, and group averages are reported in Table 2. During the control period, mean within-cluster PC was modest and mean PD was <π/2 rad. All animals showed evenly distributed patterns of PC and PD, reflected by low CV_{PC} and CV_{PD}. After L-NAME, the average number of clusters was significantly increased so that estimated cluster area was reduced. Mean PC increased and mean PD decreased while CV_{PC} and CV_{PD} increased. These results are consistent with widespread and homogeneous, although weak, synchronization of MR during control and stronger, more localized synchronization after L-NAME.

Figure 4 shows TGF synchronization, before and after L-NAME, from the same rat as in Fig. 3. During the control period, portions of two clusters are visible; mean PC was 0.72, and mean PD was 0.3π rad. Other than the magnitude of these values, the visual appearance of PC and PD was similar to MR during the control period. Low CV_{PC} (8%) and CV_{PD} (13%) were consistent with the homogeneous appearance of clusters during the control period. After L-NAME, three clusters were visible in the field of view. Within-cluster PC decreased to 0.43, and within-cluster PD increased to 0.47π rad. CV_{PC} increased to 39%, while CV_{PD} increased to 20%, confirming the increased heterogeneity of each cluster and irregular appearance within clusters.

TGF synchronization in all seven rats was similar to the animal results shown in Fig. 4, and group averages are presented in Table 2. During the control period, mean within-cluster PC was moderate and mean PD was ≈0.3π rad with homogeneous PC and PD, as shown by low CV_{PC} and CV_{PD}. L-NAME caused the number of synchronized clusters to increase while the average within-cluster PC decreased and PD increased (opposite to MR), reflecting the heterogeneous appearance of TGF clusters after L-NAME. During the control period, TGF clusters were more numerous than MR clusters ($P = 6.4 \times 10^{-6}$) and were consequently smaller (Table 2), and PC was higher in TGF clusters than in MR clusters ($P = 1.8 \times 10^{-11}$). After L-NAME, the number of TGF clusters was increased ($P = 0.008$) so that after L-NAME the number of

Downloaded from www.physiology.org/journal/ajprenal by ${individualUser.givenNames} ${individualUser.surname} (137.099.170.116) on September 1, 2018.
Copyright © 2015 American Physiological Society. All rights reserved.

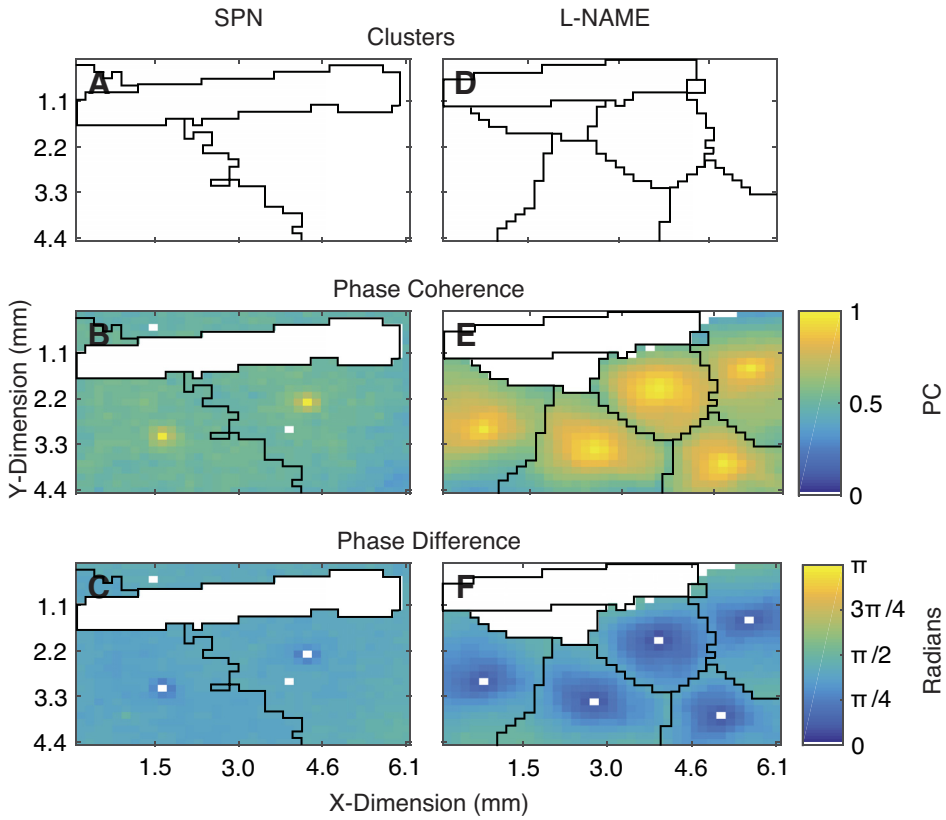

Fig. 3. Myogenic synchronization during spontaneous (SPN) control (*left*) and after N^{ω}-nitro-L-arginine methyl ester (L-NAME; *right*). The location of synchronized clusters in the field of view is shown in the *top* row (*A* and *D*). The white bar in all images masks a 4-mm scaling hair. Phase coherence between all the pixels in each cluster and the centroid of each cluster is shown in the *middle* row (*B* and *E*). The *bottom* row shows mean phase difference between the centroid of each cluster and the remaining pixels in each cluster (*C* and *F*).

TGF and MR clusters was not different ($P = 0.062$), while PC was lower in TGF clusters ($P = 0.001$).

Inspection of Figs. 3 and 4 reveals important similarities and differences between MR and TGF synchronization during control. In both cases, the small peak in PC (and minimum of PD) is an artifact resulting from correlation of the reference pixel with itself. Apart from this point, the rest of each cluster appears homogeneous with respect to PC and PD. After L-NAME, the MR clusters show a simple pattern with a broad region having high PC and low PD surrounded by a region at the cluster boundaries of low PC and high PD. In contrast, TGF clusters after L-NAME show a more complex pattern in which a small high PC, low PD region around the reference pixel is ≈4 × 4 pixels or 540 × 540 μm, larger than the artifactual centers during the control period. The rest of the cluster appears weakly synchronized (low PC and high PD). This pattern may indicate differential synchronization of smaller regions within a synchronized cluster.

Table 2. *Cluster analysis of synchronization of renal surface perfusion*

	Control	L-NAME	*P*
Field of view, $X \times Y$, mm			
X dimension	5.2 ± 0.3	5.4 ± 0.3	
Y dimension	3.8 ± 0.2	3.9 ± 0.2	
Myogenic response			
No. of clusters	1.3 ± 0.2	4.4 ± 0.5	0.0005
Estimated area, mm^2	17 ± 2	5.1 ± 0.7	0.001
PC	0.38 ± 0.03	0.57 ± 0.05	0.02
PD, rad	1.45 ± 0.04	1.20 ± 0.07	0.042
CV_{PC}	11 ± 1	16 ± 1	0.01
CV_{PD}	5 ± 1	16 ± 3	0.011
Tubuloglomerular feedback			
No. of clusters	1.7 ± 0.2	2.4 ± 0.5	0.008
Estimated area, mm^2	11 ± 1	8 ± 1	0.004
PC	0.65 ± 0.04	0.56 ± 0.05	NS
PD, rad	1.01 ± 0.09	1.31 ± 0.08	0.043
CV_{PC}	10 ± 2	17 ± 3	NS
CV_{PD}	13 ± 1	16 ± 2	NS

Values are means ± SE. Shown is a summary of dimensions of the field of view and variables arising from cluster analysis for all 7 rats. PC, phase coherence; PD, phase difference (rad); CV_{PC}, coefficient of variation for PC; CV_{PD}, coefficient of variation for PD.

Graph theory was used to further probe both scale and modularity of MR and TGF synchronization. Results from the same animal as in Figs. 3 and 4 are shown for MR in Fig. 5 and supplemental videos 1 and 2, and for TGF in Fig. 6 and supplemental videos 3 and 3 (all supplemental material for this article is accessible on the journal website). In Fig. 5, essentially no high-PC edges (PC ≥0.6) were visible during the control period. The total number of edges in this case was very high (495,667), yet there were only 62 high-PC edges as shown in Fig. 5*A*. All of those connected nearest neighbor pixels. After L-NAME, the total number of edges was reduced to 158,969 while the number of high-PC edges increased to 43,663, as shown in Fig. 5*B*. The high-PC regions seen in this panel are largely consistent with the clusters identified in Fig. 3*B*. In addition, the appearance of relatively long-distance edges is apparent across the masked portion of the field. Figure 5*D* shows that edge length is widely distributed, with some edges being 2 mm in length. Not surprisingly, there is an inverse relationship between PC and edge length. Figure 6 reveals much stronger and more widespread synchronization of TGF in the control period (Fig. 6*A*). In this case, the total

Downloaded from www.physiology.org/journal/ajprenal by ${individualUser.givenNames} ${individualUser.surname} (137.099.170.116) on September 1, 2018.
Copyright © 2015 American Physiological Society. All rights reserved.

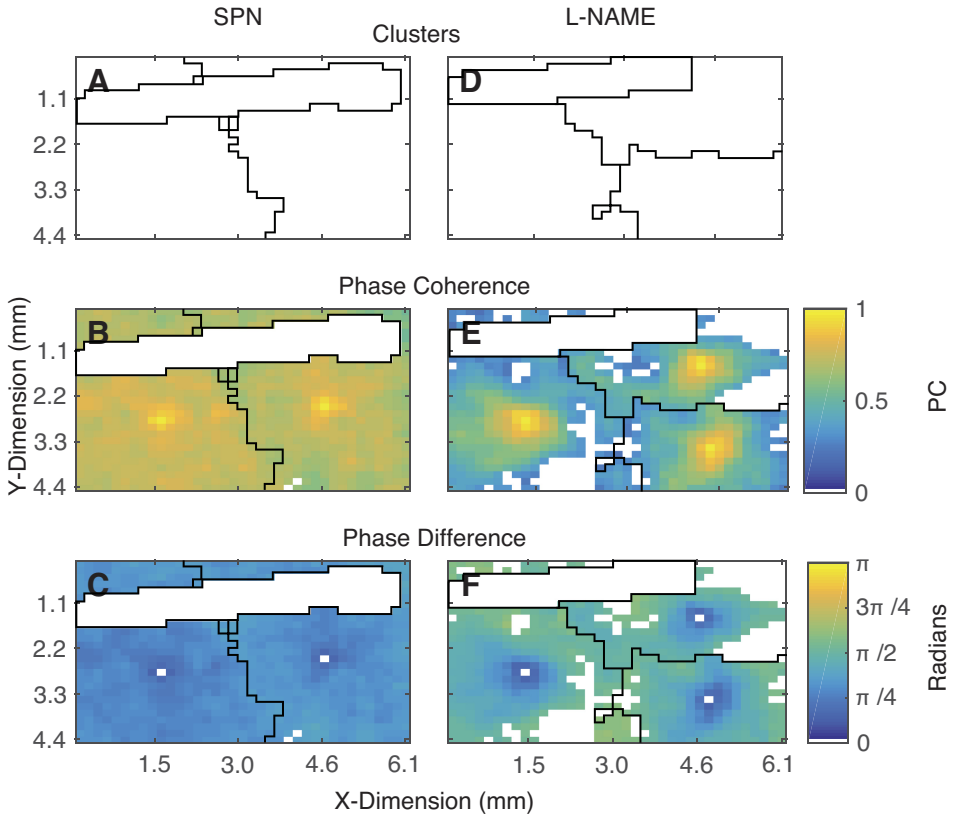

Fig. 4. Tubuloglomerular feedback synchronization before (*left*) and after (*right*) L-NAME. The location of synchronized clusters in the field of view is shown in the *top* row (*A* and *D*). The white bar in all images masks a 4-mm scaling hair. Phase coherence between all the pixels in each cluster and the centroid of each cluster is shown in the *middle* row (*B* and *E*). The *bottom* row shows mean phase difference between the centroid of each cluster and the remaining pixels in each cluster (*C* and *F*).

number of significant edges was 317,206, of which 212,372 had PC >0.6. As shown in Fig. 6*C*, edges of up to 5-mm length were observed and length was broadly distributed at all PC. Distribution of the highest PC edges in the field of view was notably inhomogeneous. After L-NAME, the total number of significant edges declined to 199,769 and the number of high PC edges was reduced to 14,214. This change was accompanied by increasing heterogeneity in the field of view so that small, high-PC regions became apparent; these regions were loosely interconnected with neighboring regions. Figure 6*D* shows that the average length of high-PC edges declined from 2.11 mm during the control period to 0.51 mm after L-NAME.

Table 3 summarizes data about edges of PC <0.6, and edges of PC >0.6. It confirms that for the MR only a small number

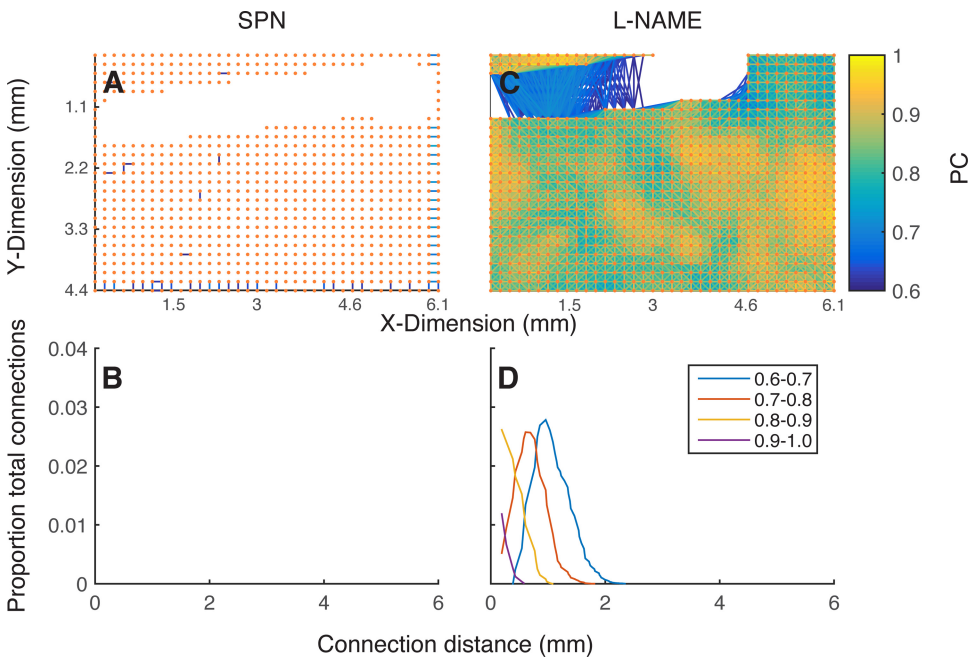

Fig. 5. Graph analysis of MR synchronization in the same animal as in Fig. 3. Each pixel is treated as a node, and PC between nodes forms the connections (edges). *A*: the almost total absence of synchronization of MR in the control period. The few edges having PC ≥0.6 connect only nearest neighbors. The lack of information in *B* shows that high-PC edges constitute a trivial fraction of total identified edges. *C*: after L-NAME, extensive synchronization develops with many long-distance edges and evident modularity. *D*: fraction of total edges and how they are distributed with PC and length.

Downloaded from www.physiology.org/journal/ajprenal by ${individualUser.givenNames} ${individualUser.surname} (137.099.170.116) on September 1, 2018.
Copyright © 2015 American Physiological Society. All rights reserved.

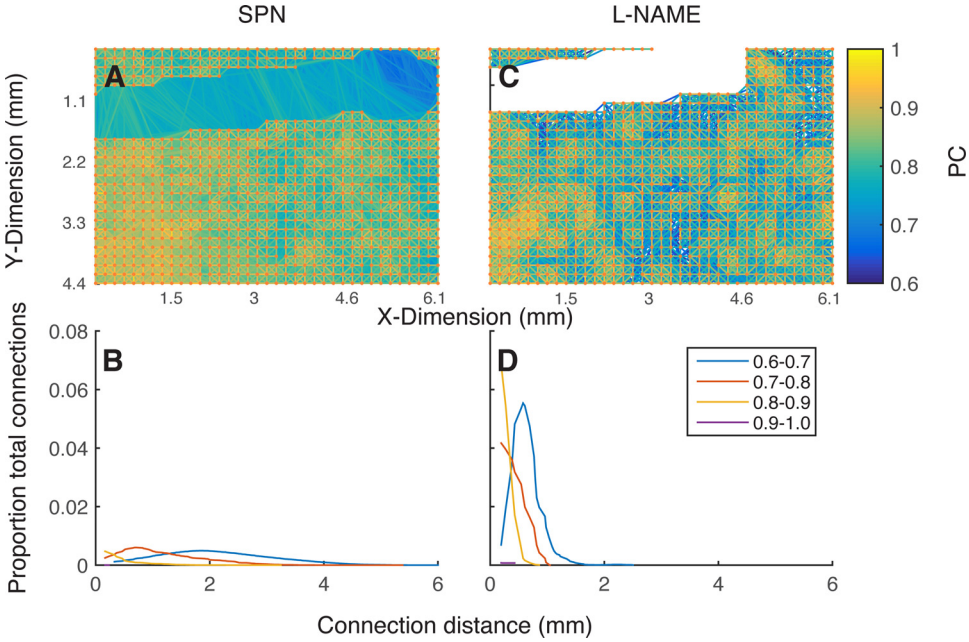

Fig. 6. Graph analysis of TGF synchronization in the same animal as in Fig. 4. Each pixel is treated as a node, and PC between nodes form the connections (edges). *A*: extensive and distinctly modular synchronization of TGF in the control period highlighting the amount of long-distance synchronization. This is confirmed in *B*, which shows broadly distributed lengths. *C*: after L-NAME, synchronization becomes increasingly modular with preferential loss of long edges (shown also in *D*). Nevertheless, the tightly synchronized modules retain significant PC with other modules over distances up to 2 mm.

of high-PC edges existed during the control period and that they were very short, typically connecting adjacent pixels. After L-NAME, both the number and length of high-PC edges increased substantially. In contrast, TGF showed large numbers of high-PC edges in the control period, and the average length of these connections approached 2 mm. Like the MR, TGF showed significant reduction of the total number of significant edges after L-NAME. While the number of high-PC edges was markedly reduced after L-NAME, the actual number and length of high-PC edges remained considerably greater for TGF than for MR.

Table 3 shows that, consistent with the images seen in Figs. 5 and 6, modularity approached 0 for MR during control, perhaps reflecting the absence of strong synchronization, and increased significantly after L-NAME. In contrast, a modular structure was evident for TGF synchronization during the control period and also increased significantly after L-NAME. Note, however, that TGF modules were both smaller and more discrete than those of MR.

Table 3. *Graph analysis of synchronization of renal surface perfusion*

	Control	L-NAME	*P*
Myogenic response			
No. of edges in field of view for low PC (<0.6)	451,589 ± 28,856	219,176 ± 46,841	0.005
No. of edges in field of view for high PC (≥0.6)	1,861 ± 1,040	43,225 ± 12,773	0.021
Length, low PC, mm	2.35 ± 0.13	1.92 ± 0.18	0.022
Length, high PC, mm	0.19 ± 0.05	0.61 ± 0.11	0.024
Modularity	0.00 ± 0.00	0.20 ± 0.05	0.018
Tubuloglomerular feedback			
No. of edges in field of view for low PC (<0.6)	161,912 ± 63,823	221,384 ± 64,616	ns
No. of edges in field of view for high PC (≥0.6)	264,460 ± 62,906	85,280 ± 31,901	0.01
Length, low PC, mm	3.34 ± 0.37	2.28 ± 0.23	0.017
Length, high PC, mm	1.89 ± 0.21	0.97 ± 0.20	0.004
Modularity	0.10 ± 0.10	0.27 ± 0.11	0.028

Values are means ± SE. Shown is a summary for all 7 rats of the quantitative analysis of graph analysis of synchronization of renal surface perfusion. Length, mean length of all edges detected in the field of view; modularity, determined after Newman (30).

DISCUSSION

The most important finding of this study is that there is large-scale, in fact macroscopic, synchronization of both TGF and MR dynamics, albeit under different conditions. Considerable modularity is present in TGF synchronization under control conditions and can be induced in the MR and enhanced in TGF by treatment with L-NAME. The modules do, however, remain significantly connected with other regions of the field, not all of which are nearest neighbors. Modularity of synchronization is more pronounced in TGF than in MR, and TGF modules have smaller dimensions, consistent with estimated cortical lobule dimensions. Thus some aspects of the current results are consistent with previous investigations of synchronization while others are noticeably different.

LSCI reports signals that are proportional to the flux of red blood cells moving just under the surface of the kidney (5, 15). The advantage of LSCI is that it assesses downstream perfusion in a reasonably large area in real time. However, it is a very noisy measurement and requires significant filtering in time and space to extract dynamic signals (heart and respiratory rates, MR, TGF) (37). The estimate of flux provided by LSCI varies tightly and linearly with other techniques for blood flow measurement including laser-Doppler flowmetry (27), capillary microscopy (3), and ultrasound flowmetry (21, 37, this study). After capturing surface perfusion, we then isolated MR and TGF dynamics to selectively probe each mechanism. The simple qualitative analysis shown in Fig. 1 demonstrates local, but not remote, synchronization of MR dynamics. The PD of the nearby ROIs in this figure is frequently zero, illustrating synchronization of separated ROIs that is stable over time. Marsh *et al.* (29) simulated TGF dynamics in a 16-nephron vascular network model and predicted exactly this

Downloaded from www.physiology.org/journal/ajprenal by ${individualUser.givenNames} ${individualUser.surname} (137.099.170.116) on September 1, 2018.
Copyright © 2015 American Physiological Society. All rights reserved.

pattern of PD in pairs of nearby nephrons. Both the prediction (29) and the data (Fig. 1) suggest that synchronization of autoregulation occurs within some spatial limits, although the limits cannot be determined from either analysis. It is trivial to point out that autoregulatory mechanisms are synchronized throughout the organism by large, and not so large, pressure transients (17). If this were the case, one would see resetting of PD to zero at a BP transient followed by divergence of PD, which could be interpreted as modest PC when averaged over time. However, the tracking phase of the synchronized pixels in Fig. 1 shows instead that PD is constant and diverges only at phase slips ($\pm 2\pi$) that tend to occur at times where the amplitude of either or both oscillations is reduced.

Cluster analysis segments the surface into synchronized clusters on a dominant spatial scale using all pairwise PC that are greater than a statistical threshold defined by surrogate data analysis. This works well for the MR under control conditions and after L-NAME, and reasonably well for TGF during control. In contrast, the appearance of TGF clusters after L-NAME indicates that they do not have a homogeneous structure. We therefore used graph theory to probe the possible modular structure of synchronization, the degree of modularity and, to some extent, the structure of that modularity. In this analysis, we treat each pixel as a node and pairwise significant PC as weighted edges connecting nodes. This allows estimation of the number of edges, their length, and their strength. It also gives a visual display of the edges (Fig. 5 and supplemental videos 1 and 2, and Fig. 6 and supplemental videos 3 and 4). In particular, the videos highlight the extensive and widespread interconnection among nodes as well as the altered connectivity and modularity induced by L-NAME.

Cluster analysis and graph theory give consistent and complementary information about synchronization, both under control conditions and after L-NAME. Both analyses capture autoregulation dynamics (23, 48, 50), and both show that L-NAME substantially enhances MR synchronization and that it alters the pattern of TGF synchronization. Furthermore, cluster analysis and graph theory identify the same highly connected regions in the field of view.

Only two previous studies have examined MR synchronization. Sosnovtseva et al. (41) examined data from micropuncture studies and showed synchronized MR in local but not remote arteriole pairs. Scully et al. (36) used LSCI and showed very similar results to those reported here for MR synchronization, with the same cluster analysis. Most previous studies of TGF synchronization involved micropuncture determination of tubular pressure. These studies by Marsh and colleagues demonstrated synchronization of TGF (11, 19, 52) and MR (41) dynamics in pairs of nephrons, but did not identify synchronization over larger scales. A limitation of micropuncture is that the potential number of oscillators that can be probed is very small and that MR signals, at least, are heavily filtered. In contrast, LSCI acquires data from a large fraction of the cortical surface, permitting assessment of potential distributed function. Successive analyses of a limited number of micropuncture datasets have employed progressively more sensitive techniques, culminating in wavelet-based detection of phase coherence. As shown in Fig. 2, analysis based on the Hilbert transform outperforms the wavelet technique (21) in detecting phase coherence at low signal-to-noise ratio. While subsequent developments have improved sensitivity of wavelet-based detection (7), the Hilbert-based detection of phase used here will detect synchronization that would have been missed by previous analyses.

The first LSCI study assessed TGF synchronization in identified efferent arterioles at the surface (star vessels) using wavelet-based detection of frequency coupling (21). Hierarchical clustering was used to establish synchronization and was interpreted, conservatively, in terms of intralobular synchronization. Interestingly, hierarchical clustering is another term for modularity (30), and Fig. 6 in Ref. 21 suggests the presence of modules. A more recent study by these authors (7) segmented the surface based on phase coherence, but imposed a prior condition on the determination of PC based on the expectation that synchronization is local only. Even so, surprisingly large synchronized clusters were identified in some animals. In the present study, we wished to examine synchronization of both TGF and MR. This required use of the 25-Hz, low-spatial resolution mode of the instrument because of potential aliasing problems. Therefore, we were unable to resolve individual star vessels and instead treated the image as a flow field. We used cluster analysis without prior conditions to identify synchronized regions of both MR and TGF. A second and independent analysis using graph theory confirmed the major conclusions from the cluster analysis and emphasized both the magnitude (number of edges) and the extent of distribution (length of edges) of synchronization of both MR and TGF.

Based on known TGF synchronization within lobules (11, 19, 52), measured mechanical length constants (42, 47), and vascular anatomy (2, 6), we proposed that the lobule would form the minimum synchronized unit of autoregulation. While qualitative description of cortical vascular anatomy is excellent, there is little quantitative information available in the literature about the dimensions of cortical lobules. We have chosen to use an estimate provided by Prof. W. Kriz (personal communication) that the spacing between cortical radial arteries is between 0.5 and 0.7 mm and that lobular surface profiles are often quadrilateral. We thus estimate the lobular surface area to be 0.3–0.5 mm^2 and large enough, $\geq 4 \times 4$ pixels or ≈ 0.3 mm^2, to be detected reliably (36). The homogeneous distribution of PC within TGF clusters during the control period, combined with the large number and length of PC edges, suggests that TGF, despite its local origin, might well be considered a distributed network behavior. Graph analysis revealed a modular structure of TGF synchronization in the control period that increased after L-NAME and suggests an important role for lobules as organizing centers. In contrast, the larger and more diffuse modules seen in MR synchronization after L-NAME are more likely to be organized around variations in arterial topology or geometry.

It is increasingly apparent that many biological processes are organized as distributed networks, including but not limited to cerebral processing (14, 22), endocrine control (44), and regulation of blood flow in microcirculations (33, 38). Studies in other microcirculations indicate that maintaining stable downstream blood flow in a tree structure requires coordinated adjustment in all axially connected upstream segments and in branches thereof (reviewed in Refs. 32, 33, and 38). The renal circulation displays strong axial communication via endothelial gap junctions (40). We show large-scale information exchange by both MR and TGF over surprisingly long distances. Modularity was expected and certainly demonstrated with

Downloaded from www.physiology.org/journal/ajprenal by ${individualUser.givenNames} ${individualUser.surname} (137.099.170.116) on September 1, 2018.
Copyright © 2015 American Physiological Society. All rights reserved.

intensely coupled modules (short, high-PC edges). However, the number of edges connecting modules remained substantial in both MR and TGF. The extent of long-distance communication indicates that synchronization occurs on a scale that was not predicted by previous experimental and simulation studies. We feel the demonstration of widespread, long-distance synchronization argues strongly that renal autoregulation is a distributed process which can be expected to provide considerable smoothing of perfusion in space (46). Furthermore, considerable plasticity of synchronization of both TGF and MR is demonstrated, suggesting that there is the capacity to adjust to a variety of internal or environmental conditions.

There are several limitations to this study. Estimation of PC significance requires 30–50 cycles of the oscillators in question to separate real from factitious synchronization, thus limiting the study to quasi-steady-state estimates of synchronization (36). Thus we cannot tell whether the inverse relationship between PC and edge length results from noise or from time-varying behavior. Clearly, this needs to be addressed in future studies. Although we can detect transients where PD slips ($\pm 2\pi$), we could not exclude the likelihood that long-distance PC is weaker simply due to axial signal degeneration or introduction into the signal pathway of multiple other signals. There is also the question of how multiple lobules achieve TGF synchronization since juxtamedullary nephrons have lower TGF frequencies (20) that could desynchronize neighboring lobules. Given that the frequency of TGF is labile (12, 53) (Fig. 1), that transit time through the loop of Henle can vary (43, 45), and that synchronization is clearly plastic, it is possible that there is m:n synchronization of TGF between juxtamedullary nephrons and the short-looped nephrons in several m:n (e.g., 2:3) frequency ratios.

ACKNOWLEDGMENTS

Present address of K. H. Chon: Univ., of Connecticut, Biomedical Engineering Department, A. B. Bronwell Bldg., Rm. 217, 260 Glenbrook Rd., Unit 3247, Storrs, CT 06269-3247.

Present address of C. G. Scully: Office of Science and Engineering Laboratories, Center for Devices and Radiological Health, US Food and Drug Administration, 10903 New Hampshire Ave. WO62-3617, Silver Spring, MD 20993-0002.

GRANTS

This work was supported by Canadian Institutes of Health Research Grant MOP-102694 (to W. A. Cupples, B. Braam, and K. H. Chon). N. Mitrou was supported in part by Graduate Fellowships from the Department of Biomedical Physiology and Kinesiology. C. G. Scully was supported by a predoctoral fellowship from the American Heart Association. B. Braam was supported by a Heart and Stroke Foundation of Canada New Investigator award during these studies.

DISCLOSURES

No conflicts of interest, financial or otherwise, are declared by the authors.

AUTHOR CONTRIBUTIONS

Author contributions: N.M. performed experiments; N.M., C.G.S., and K.H.C. analyzed data; N.M., C.G.S., B.B., and W.A.C. interpreted results of experiments; N.M. prepared figures; N.M. and W.A.C. drafted manuscript; N.M., C.G.S., B.B., K.H.C., and W.A.C. approved final version of manuscript; C.G.S., B.B., K.H.C., and W.A.C. edited and revised manuscript; B.B. and W.A.C. provided conception and design of research.

REFERENCES

1. **Balanov A, Janson N, Postnov DD, Sosnovtseva OV.** *Synchronization: From Simple to Complex*. Berlin: Springer-Verlag, 2009.
2. **Beeuwkes R, III, Bonventre JV.** Tubular organization and vascular tubular relations in the dog kidney. *Am J Physiol* 229: 695–713, 1975.
3. **Bezemer R, Legrand M, Klijn E, Heger M, Post I, van Gulik TM, Payen D, Ince C.** Real-time assessment of renal cortical microvascular perfusion heterogeneities using near-infrared laser speckle imaging. *Optics Express* 18: 15054–15061, 2010.
4. **Blinder P, Tsai PS, Kaufhold JP, Knutsen PM, Suhl H, Kleinfeld D.** The cortical angiome: an interconnected vascular network with noncolumnar patterns of blood flow. *Nat Neurosci* 16: 889-U150, 2013.
5. **Boas DA, Dunn AK.** Laser speckle contrast imaging in biomedical optics. *J Biomed Opt* 15: 011109, 2010.
6. **Braus H.** *Anatomie des Menschen: Zweiter Band Eingeweide*. Berlin: Springer, 1924.
7. **Brazhe AR, Marsh DJ, Holstein-Rathlou NH, Sosnovtseva O.** Synchronized renal blood flow dynamics mapped with wavelet analysis of laser speckle flowmetry data. *PLoS One* 9: e105879, 2014.
8. **Brown DM, Provoost AP, Daly MJ, Lander ES, Jacob HJ.** Renal disease susceptibility and hypertension are under independent genetic control in the fawn-hooded rat. *Nat Genet* 12: 44–51, 1996.
9. **Bryden J, Funk S, Geard N, Bullock S, Jansen VAA.** Stability in flux: community structure in dynamic networks. *J R Soc Interface* 8: 1031–1040, 2011.
10. **Casellas D, Dupont M, Bouriquet N, Moore LC, Artuso A, Mimran A.** Anatomic pairing of afferent arterioles and renin cell distribution in rat kidneys. *Am J Physiol Renal Fluid Electrolyte Physiol* 267: F931–F936, 1994.
11. **Chen YM, Yip KP, Marsh DJ, Holstein-Rathlo NH.** Magnitude of TGF-initiated nephron-nephron interactions is increased in SHR. *Am J Physiol Renal Fluid Electrolyte Physiol* 269: F198–F204, 1995.
12. **Chon KH, Zhong Y, Moore LC, Holstein-Rathlou NH, Cupples WA.** Analysis of nonstationarity in renal autoregulation mechanisms using time-varying transfer and coherence functions. *Am J Physiol Regul Integr Comp Physiol* 295: R821–R828, 2008.
13. **Cupples WA, Novak P, Novak V, Salevsky FC.** Spontaneous blood pressure fluctuations and renal blood flow dynamics. *Am J Physiol Renal Fluid Electrolyte Physiol* 270: F82–F89, 1996.
14. **Doesburg SM, Vidal J, Taylor MJ.** Reduced theta connectivity during set-shifting in children with autism. *Front Hum Neurosci* 7: doi:10.3389/fnhum.2013.00785, 2013.
15. **Forrester KR, Tulip J, Leonard C, Stewart C, Bray RC.** A laser speckle imaging technique for measuring tissue perfusion. *IEEE Trans Biomed Eng* 51: 2074–2084, 2004.
16. **Guyton AC, Hall JE.** *Textbook of Medical Physiology*. Philadelphia, PA: Saunders, 2006.
17. **Guyton AC, Langston JB, Navar G.** Theory for renal autoregulation by feedback at the juxtaglomerular apparatus. *Circ Res* 15: 187–197, 1964.
18. **Hayashi K, Epstein M, Loutzenhiser R.** Pressure-induced vasoconstriction of renal microvessels in normotensive and hypertensive rats: studies in the isolated perfused hydronephrotic kidney. *Circ Res* 65: 1475–1484, 1989.
19. **Holstein-Rathlou NH.** Synchronization of proximal tubular pressure oscillations: evidence for interaction between nephrons. *Pflügers Arch* 408: 438–443, 1987.
20. **Holstein-Rathlou NH, Marsh DJ.** Oscillations of tubular pressure, flow, and distal chloride concentration in rats. *Am J Physiol Renal Fluid Electrolyte Physiol* 256: F1007–F1014, 1989.
21. **Holstein-Rathlou NH, Sosnovtseva OV, Pavlov AN, Cupples WA, Sorensen CM, Marsh DJ.** Nephron blood flow dynamics measured by laser speckle contrast imaging. *Am J Physiol Renal Physiol* 300: F319–F329, 2011.
22. **Hubel DH, Wiesel TN.** Brain mechanisms of vision. *Sci Am* 241: 150–162, 1979.
23. **Just A, Ehmke H, Wittmann U, Kirchheim HR.** Tonic and phasic influences of nitric oxide on renal blood flow autoregulation in conscious dogs. *Am J Physiol Renal Physiol* 276: F442–F449, 1999.
24. **Just A, Wittmann U, Ehmke H, Kirchheim HR.** Autoregulation of renal blood flow in the conscious dog and the contribution of the tubuloglomerular feedback. *J Physiol (Lond)* 506: 275–290, 1998.
25. **Kallskog O, Marsh DJ.** TGF-initiated vascular interactions between adjacent nephrons in the rat kidney. *Am J Physiol Renal Fluid Electrolyte Physiol* 259: F60–F64, 1990.
26. **Krupatkin AI.** Oscillatory structures of blood flow reflect the dynamics of information processes in microcirculatory networks. *Hum Physiol* 36: 211–221, 2010.

Downloaded from www.physiology.org/journal/ajprenal by ${individualUser.givenNames} ${individualUser.surname} (137.099.170.116) on September 1, 2018.
Copyright © 2015 American Physiological Society. All rights reserved.

27. **Legrand M, Bezemer R, Kandil A, Demirci C, Payen D, Ince C.** The role of renal hypoperfusion in development of renal microcirculatory dysfunction in endotoxemic rats. *Intensive Care Med* 37: 1534–1542, 2011.
28. **Lopez B, Ryan RP, Moreno C, Sarkis A, Lazar J, Provoost AP, Jacob HJ, Roman RJ.** Identification of a QTL on chromosome 1 for impaired autoregulation of RBF in fawn-hooded hypertensive rats. *Am J Physiol Renal Physiol* 290: F1213–F1221, 2006.
29. **Marsh DJ, Wexler AS, Brazhe A, Postnov DE, Sosnovtseva OV, Holstein-Rathlou NH.** Multinephron dynamics on the renal vascular network. *Am J Physiol Renal Physiol* 304: F88–F102, 2013.
30. **Newman MEJ.** Modularity and community structure in networks. *Proc Natl Acad Sci USA* 103: 8577–8582, 2006.
31. **Pikovsky AS, Rosenblum MG, Kurths J.** *Synchronization: A Universal Concept in Nonlinear Science*. Cambridge, UK: Cambridge Univ. Press, 2001.
32. **Pradhan RK, Chakravarthy VS.** Informational dynamics of vasomotion in microvascular networks: a review. *Acta Physiol (Oxf)* 201: 193–218, 2011.
33. **Pries AR, Hopfner M, le Noble F, Dewhirst MW, Secomb TW.** The shunt problem: control of functional shunting in normal and tumour vasculature. *Nat Rev Cancer* 10: 587–593, 2010.
34. **Rivers RJ.** Remote effects of pressure changes in arterioles. *Am J Physiol Heart Circ Physiol* 268: H1379–H1382, 1995.
35. **Scully CG.** *Detection of Spatial and Temporal Interactions in Renal Autoregulation Dynamics* (Dissertation). Worcester, MA: Worcester Polytechnic Institute, 2013.
36. **Scully CG, Mitrou N, Braam B, Cupples WA, Chon KH.** Segmentation of renal perfusion signals from laser speckle imaging into clusters with phase synchronized dynamics. *IEEE Trans Biomed Eng* 61: 19890–11997, 2014.
37. **Scully CG, Mitrou NGA, Braam B, Cupples WA, Chon KH.** Detecting physiological systems with laser speckle perfusion imaging of the renal cortex. *Am J Physiol Regul Integr Comp Physiol* 304: R929–R939, 2013.
38. **Secomb TW, Pries AR.** Information transfer in microvascular networks. *Microcirculation* 9: 377–387, 2002.
39. **Shi Y, Wang X, Chon KH, Cupples WA.** Tubuloglomerular feedback-dependent modulation of renal myogenic autoregulation by nitric oxide. *Am J Physiol Regul Integr Comp Physiol* 290: R982–R991, 2006.
40. **Sorensen CM, Holstein-Rathlou NH.** Cell-cell communication in the kidney microcirculation. *Microcirculation* 19: 451–460, 2012.
41. **Sosnovtseva OV, Pavlov AN, Mosekilde E, Yip KP, Holstein-Rathlou NH, Marsh DJ.** Synchronization among mechanisms of renal autoregulation is reduced in hypertensive rats. *Am J Physiol Renal Physiol* 293: F1545–F1555, 2007.
42. **Steinhausen M, Endlich K, Nobiling R, Parekh N, Schutt F.** Electrically induced vasomotor responses and their propagation in rat renal vessels in vivo. *J Physiol (Lond)* 505: 493–501, 1997.
43. **Steinhausen M, Hill E, Parekh N.** Intravital microscopical studies of tubular urine flow in conscious rat. *Pflügers Arch* 362: 261–264, 1976.
44. **Stevens A, De Leonibus C, Hanson D, Dowsey AW, Whatmore A, Meyer S, Donn RP, Chatelain P, Banerjee I, Cosgrove KE, Clayton PE, Dunne MJ.** Network analysis: a new approach to study endocrine disorders. *J Mol Endocrinol* 52: R79–R93, 2014.
45. **Stumpe KO, Lowitz HD, Ochwadt B.** Fluid reabsorption in Henle's loop and urinary excretion of sodium and water in normal rats and rats with chronic hypertension. *J Clin Invest* 49: 1200–1212, 1970.
46. **Tran CHT, Vigmond EJ, Goldman D, Plane F, Welsh DG.** Electrical communication in branching arterial networks. *Am J Physiol Heart Circ Physiol* 303: H680–H692, 2012.
47. **Wagner AJ, Holstein-Rathlou NH, Marsh DJ.** Internephron coupling by conducted vasomotor responses in normotensive and spontaneously hypertensive rats. *Am J Physiol Renal Physiol* 272: F372–F379, 1997.
48. **Wang X, Cupples WA.** Interaction between nitric oxide and renal myogenic autoregulation in normotensive and hypertensive rats. *Can J Physiol Pharmacol* 79: 238–245, 2001.
49. **Wang X, Loutzenhiser RD, Cupples WA.** Frequency modulation of renal myogenic autoregulation by perfusion pressure. *Am J Physiol Regul Integr Comp Physiol* 293: R1199–R1204, 2007.
50. **Wang X, Salevsky FC, Cupples WA.** Nitric oxide, atrial natriuretic factor, and dynamic renal autoregulation. *Can J Physiol Pharmacol* 77: 777–786, 1999.
51. **Woods LL.** Mechanisms of renal hemodynamic regulation in response to protein feeding. *Kidney Int* 44: 659–675, 1993.
52. **Yip KP, Holstein-Rathlou NH, Marsh DJ.** Dynamics of TGF-initiated nephron-nephron interactions in normotensive rats and SHR. *Am J Physiol Renal Fluid Electrolyte Physiol* 262: F980–F988, 1992.
53. **Zou R, Cupples WA, Yip KP, Holstein-Rathlou NH, Chon KH.** Time-varying properties of renal autoregulatory mechanisms. *IEEE Trans Biomed Eng* 49: 1112–1120, 2002.

Downloaded from www.physiology.org/journal/ajprenal by ${individualUser.givenNames} ${individualUser.surname} (137.099.170.116) on September 1, 2018.
Copyright © 2015 American Physiological Society. All rights reserved.